Journal of
Mechanics of
Materials and Structures

MECHANICS OF POLYCARBONATE DURING HIGH-RATE TENSION

Sai S. Sarva and Mary C. Boyce

Volume 2, Nº 10 December 2007

mathematical sciences publishers

JOURNAL OF MECHANICS OF MATERIALS AND STRUCTURES
Vol. 2, No. 10, 2007

MECHANICS OF POLYCARBONATE DURING HIGH-RATE TENSION

SAI S. SARVA AND MARY C. BOYCE

Polymeric materials often undergo large inhomogeneous deformations at high rates during their use in various impact-resistant energy-absorbing applications. For better design of such structures, a comprehensive understanding of high-rate deformation under various loading modes is essential. In this study, the behavior of polycarbonate was studied during tensile loading at high strain rates, using a split-collar type split Hopkinson tension bar (SHTB). The effects of varying strain rate, overall imposed strain magnitude and specimen geometry on the mechanical response were examined. The chronological progression of deformation was captured with a high-speed rotating mirror CCD camera. The deformation mechanics were further studied via finite element simulations using the ABAQUS/Explicit code together with a recently developed constitutive model for high-rate behavior of glassy polymers. The mechanisms governing the phenomena of large inhomogeneous elongation, single and double necking, and the effects of material constitutive behavior on the characteristics of tensile deformation are presented.

1. Introduction

Polymeric materials are known to exhibit strong strain-rate sensitivity in many aspects of mechanical behavior including initial stiffness, yield stress, post-yield behavior and final failure. The mechanisms governing this rate dependence are particularly pronounced at very high rates, such as those occurring during impact loading events. Polymers are also known to exhibit a difference in properties in tension when compared to compression, where the yield stress depends on the pressure [Argon 1973; Spitzig and Richmond 1979; Caddell and Kim 1981], and the post-yield strain hardening depends on the developing molecular orientation [Arruda and Boyce 1993]. The compressive and tensile behavior of polymers has been widely studied under quasistatic conditions. The high-rate compressive behavior of polymers has been a topic of recent investigation by several groups [Walley and Field 1994; Moy et al. 2003; Mulliken and Boyce 2004, 2006; Sivior et al. 2005; Richeton et al. 2006]. In contrast, the high-rate tensile behavior has not been thoroughly studied due to the complex nature of the experimental techniques. However, it is important that the tensile properties be accurately evaluated to gather a complete understanding of the mechanics governing deformation at high rates and to help improved physics-based constitutive modeling of the high-rate behavior. In particular, a polymer which may deform in a ductile manner at low rates in tension may become brittle at high rates.

Keywords: dynamic tension, Hopkinson bar, polycarbonate, multiple necking, finite element modeling, ABAQUS.
This research was supported by the AFOSR through Defense University Research Initiative on Nanotechnology, under contract No. F49620-01-1-0447 and the ONR through contract No. N00014-04-10469 and, in part, by the Dupont–MIT Alliance. The authors acknowledge the high-rate test facilities of the MIT Institute for Soldier Nanotechnologies.

1.1. ***Background.*** The mechanical behavior of materials at high rates has been extensively studied over the past half of a century using numerous experimental procedures ranging from Taylor impact to split Hopkinson pressure bar (SHPB) to flyer-plate impact tests. Amongst these procedures, SHPB testing has been instrumental in obtaining high-rate stress-strain behavior. The history and theory of the SHPB are well documented [Kolsky 1963; Follansbee 1985; Gray 2000]. The basic design of a SHPB consists of a specimen sandwiched between two long rods, called the incident (or input) bar and the transmission (or output) bar. A shorter striker bar is impacted on to the incident bar, sending an elastic compressive pulse down the bar to the sample; this pulse gets partly reflected and partly transmitted due to the impedance mismatch between the bars and the sample. The incident, reflected, and transmitted pulses are measured using strain gauges attached to the bars and the stress-strain behavior of the sample is calculated using one-dimensional elastic wave theory. Though initially used for compression testing of metals, nominally at strain rates up to $10^4\ s^{-1}$, the SHPB has since been modified by many researchers to extend its capabilities to test a complete spectrum of materials (ceramics, polymeric/soft materials, composites), and a range of loading modes (tension, torsion); for some relevant examples, see [Chen et al. 1999; 2000; Gray 2000; Gray and Blumenthal 2000; Field et al. 2004].

High-rate studies of polymers in compression with the SHPB are further complicated due to their low density, low modulus and low yield stress. The low densities and low elastic wave velocities ultimately result in low impedances. The low impedance results in low amplitude of transmitted pulses, which increases the signal-to-noise ratio. To address these problems, many modifications have been suggested by various researchers. Low impedance bars made of titanium and magnesium have been used by Gray et al.[1997; 1998]. Polymeric bars have also been used to help reduce the impedance mismatch between the sample and the bars, thus increasing the magnitude of transmitted pulses [Wang et al. 1994; Zhao and Gary 1995; Sawas et al. 1998]. Chen et al. [1999] incorporated a hollow aluminum transmission bar to reduce the cross-sectional area ratio between the sample and the bar and improve the signal magnitude.

The earliest design changes to the SHPB to enable tensile loading conditions were made by Harding et al. [1960] during studies of metal alloys. In this design, the specimen is threaded between the incident and transmission bars and a tensile pulse is directly generated in the incident bar. One method of generating the tensile pulse incorporates a flange on the free end of the incident bar and a hollow striker bar that surrounds the incident bar. The striker bar is propelled towards the flange (in the direction away from the sample) to induce the incident tensile pulse. The principles of data analysis for the tensile tests are the same as those for compressive tests. An alternate design by Lindholm and Yeakley [1968] incorporates a solid incident bar and a hollow transmission bar. The inner diameter of the transmission bar is larger than the incident bar. A hat-shaped specimen is sandwiched between the bars such that the top of the hat rests on the end of the incident bar. The incident bar along with the sample then slides into the transmission bar until the brim of the hat rests against the hollow transmission bar. Upon the passing of a compressive pulse, the sample is loaded such that the sides of the hat are stressed in tension. Data analysis is again similar to compressive tests. The drawbacks for this design arise mainly from complexities due to the specimen geometry.

In a third design by Nicholas [1981], a threaded sample is attached between the two bars; a split collar surrounds the sample and is snugly sandwiched between the two bars. This collar enables the transmission of the initial compressive pulse into the second bar without loading the sample. The subsequent reflected tensile pulse (from the free rear end of the second bar) then loads the sample. This design is

desirable for its simplicity and has been used for the present studies. It is discussed further in Section 2.1. The experimental difficulties in high-rate tensile testing are compounded by the large lengths and, often, the necessity to use samples of complex shapes. (Henceforth, we shall refer to a sample's gauge length more simply as its length and similarly refer to its gauge diameter as its diameter.) The large lengths increase the duration to attain dynamic equilibrium, invalidating a large portion of acquired data. Often pulse shaping techniques are necessary to increase the rise time of the loading pulses, delay the yield event until after dynamic equilibrium, and improve the quality of data. Also, large lengths limit the attaining of very large strain rates. Furthermore, as with all tensile tests, once specimen necking occurs, the data is not easily reduced to material stress-strain data.

Recently, a few studies have explored the testing of polymers under dynamic tension. Chen et al. [2002] studied the dynamic tensile behavior of Epon 828/T-403 epoxy and poly(methyl methacrylate) (PMMA) at strain rates up to $1200\,s^{-1}$ using a SHTB with a hollow transmission bar. They noted that failure strains in dynamic tension were lower than during static tests; these two materials are brittle in tension and the failure strains were in the 5% range. Cheng and Chen [2003] studied the tensile stress-stretch behavior of ethylene-propylene-diene ter polymer (EPDM rubber) at stretching rates of 2800–$3200\,s^{-1}$ and demonstrated that the mechanical properties depended significantly on the stretching rate and that a Mullins effect (cyclic softening) also occurs under dynamic conditions. Rae and Brown [2005] studied properties of poly(tetrafluoroethylene) in high-rate tension with the help of a SHTB incorporated with a titanium transmission bar and observed moderate strain-rate and temperature sensitivity.

Significant advances have also been made in modeling the large strain, temperature, and rate-dependent constitutive behavior of glassy polymers and the underlying deformation micro-mechanisms [Boyce et al. 1988; Arruda and Boyce 1993; Arruda et al. 1995]. Mulliken and Boyce [2004; 2006] have recently further enhanced these previous constitutive models to incorporate mechanisms that are activated during high loading rates. An overview of micro-mechanisms of high-rate behavior of amorphous polymers is provided in Section 2.2.1. The uniaxial tensile behavior of PC at rates exceeding $1000\,s^{-1}$ is then presented using a SHTB facility designed and built for this purpose. The SHTB tests are numerically simulated and understood utilizing finite element analysis together with the physically based high-rate constitutive model of Mulliken and Boyce [2006].

2. Investigation protocol

2.1. *Experimental procedures.*

2.1.1. *Split-collar SHTB.* A split collar type SHTB was used for the present studies; Figure 1 shows a schematic of the SHTB setup. 7075-T6 aluminum bars (diameter = 19.75 mm) were chosen to minimize the bar-polymer sample impedance mismatch and enhance the signal-to-noise ratio. The rear/second bar (1.524 m) was shorter than the front/first bar (3.048 m) and both contained threaded holes to accommodate samples. A representative sample geometry is shown in Figure 1. The striker bar was approximately 48 cm in length and propelled using a pneumatic punch. The impact velocities of the striker bar were of the order of $20\,ms^{-1}$. The split collar (diameter = 25.4 mm; inner diameter = 12.7 mm) was tightly sandwiched between the bars, encompassing the sample. Upon impact of the striker bar, a compressive pulse lasting approximately 200 μs is generated in the first bar and travels down the length of the bar. On reaching the split collar, it shunts the sample and travels through the collar into the rear bar. In

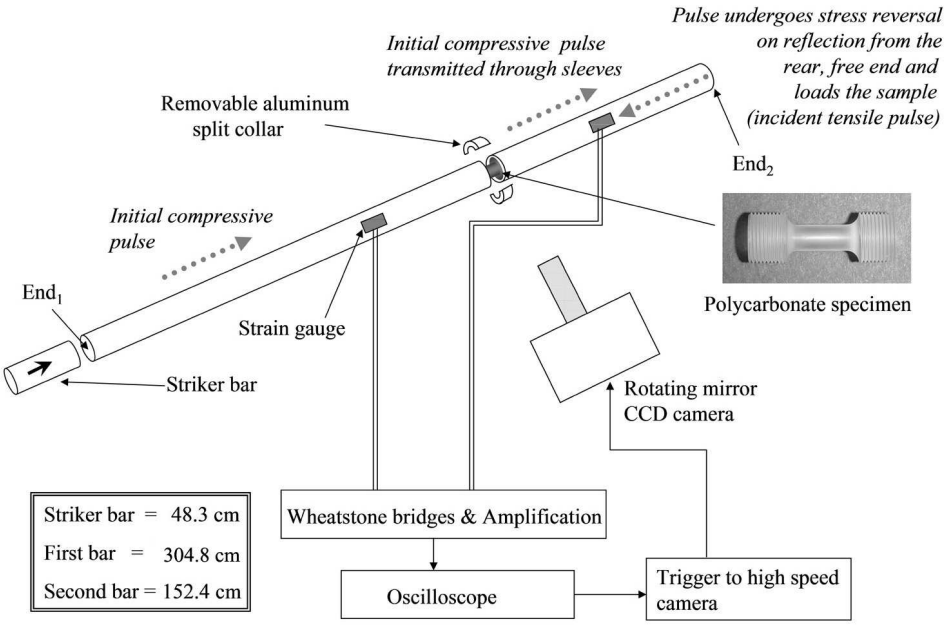

Figure 1. Schematic of the split-collar SHTB.

practice, it is not possible to prevent prestraining the sample; however, any prestraining is well below the elastic limit. The cross sectional area of the collar was chosen such that the initial compressive pulse was mostly transferred to the rear bar. Though a small portion of the initial pulse was reflected from the first bar-collar interface, the length of the first bar and the position of the strain gauges were such that this portion of the pulse and its subsequent reflection from the free end of the first bar (End_1 in Figure 1) did not interfere with the recording of the test data. The compressive pulse transmitted through the collar undergoes stress reversal upon rebounding from the free end of the rear bar (End_2 in Figure 1). The smaller rear bar length helps reduce the distance the tensile pulse travels to reach the sample, thus minimizing its dispersive distortion. Upon reaching the sample, the pulse loads the sample in tension, whereas the collar that is not physically joined to the bars remains unloaded. So, in effect, the rear bar acts as the 'incident bar' and the front bar acts as the 'transmission bar'. The samples were machined to attach tightly to the bars. Also, pure annealed copper pulse shapers were placed at End_1 to cushion the impact of the striker bar. The pulse shaper lengthened the rise time considerably, leading to a delay in attaining peak stresses, thus improving dynamic equilibrium in the sample and also dampening the high frequency oscillations in the pulses [Gray and Blumenthal 2000].

The incident tensile, reflected, and transmitted pulses were measured with strain gauges attached on the bars at appropriate lengths. The gauge signals were routed through a Vishay 2100 strain gauge conditioner and amplifier system. The frequency response of the conditioner was extended to 50 kHz. The signals were acquired using a Lecroy Waverunner 14 bit oscilloscope. Figure 2 shows the raw strain gauge-signals gathered from separate strain gauges on the two bars. A small portion of the initial pulse that reflects from the bar-collar interface is also shown.

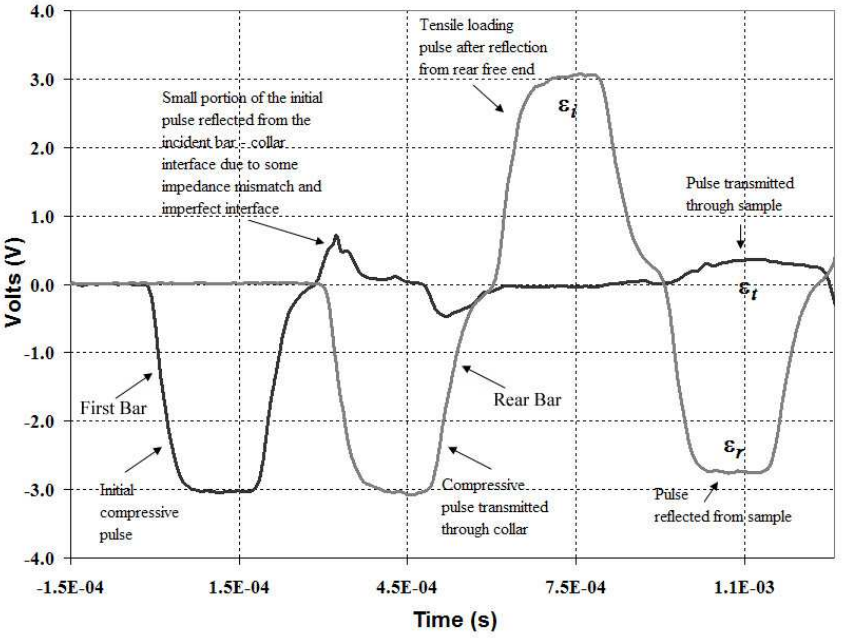

Figure 2. Raw strain gauge signals acquired during a dynamic tension test.

The axial force-displacement for the front and rear ends of the sample can be calculated from the incident ϵ_i, reflected ϵ_r and transmitted ϵ_t pulses using the relationships detailed here. The end displacements are

$$u_1 = c_0 \int (\epsilon_i - \epsilon_r) dt \qquad u_2 = c_0 \int \epsilon_t dt.$$

Similarly the forces on the ends are:

$$F_1 = E A_0 (\epsilon_i + \epsilon_r), \qquad F_2 = E A_0 \epsilon_t.$$

The force calculations on the two ends can be compared to verify how long it takes to achieve dynamic equilibrium during a test. Figure 3 shows a comparison of forces at the incident and transmitted ends, calculated using $(\epsilon_i + \epsilon_r)$ and ϵ_t, respectively. Additionally, the above relationships also help calculate the time-resolved velocities of the end surfaces, which can be used as boundary conditions for finite element simulations. Figure 4 shows the velocity profiles of the incident bar-specimen interface and transmission bar-specimen interface during a sample test.

2.1.2. *High-speed photography.* A Cordin 550 rotating mirror high-speed CCD camera with a Nikon 100 mm macro lens, capable of acquiring images at a frame rate of 2 million frames per second, was used to photograph the dynamic deformation of tensile samples. Because the collar encompasses the specimen, front and back windows were machined into the collar halves to help view the sample. Also, for samples with smaller lengths, a C-shaped collar was used to help photograph the sample. The camera was triggered via the oscilloscope, which had sent out a rising edge TTL trigger pulse after it had been

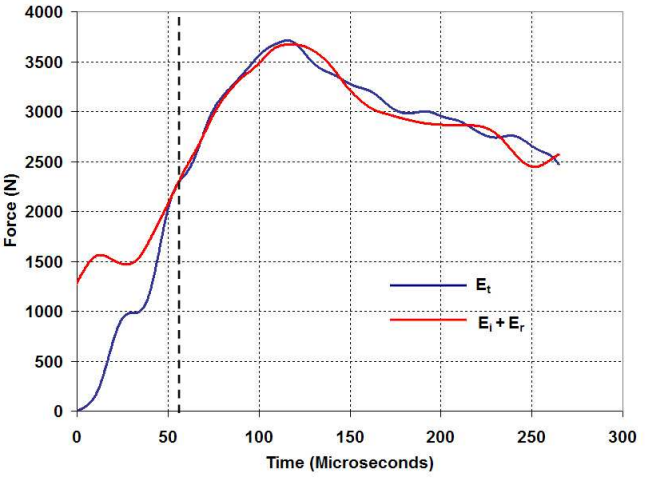

Figure 3. Sample time-resolved force signals calculated using $\epsilon_i + \epsilon_r$ and ϵ_t during a dynamic tension test.

triggered by the incident strain gauge pulse. A built-in trigger delay was used to synchronize the capture of images with the tensile test. The camera in turn triggered a high performance strobe for better illumination, which was placed behind the specimen for silhouette lighting of the specimen. The camera was programmed to record a sequence of 32 separate images at prescribed time intervals, and images were acquired from a point of view normal to the specimen.

2.1.3. *Sample design.* PC was chosen for the study due to its excellent combination of stiffness, strength, toughness, ductility, impact resistance, and transparency. Machine-grade PC was procured from GE Polymershapes in the form of a 12.7 mm diameter extruded rod. Threaded samples with varying length

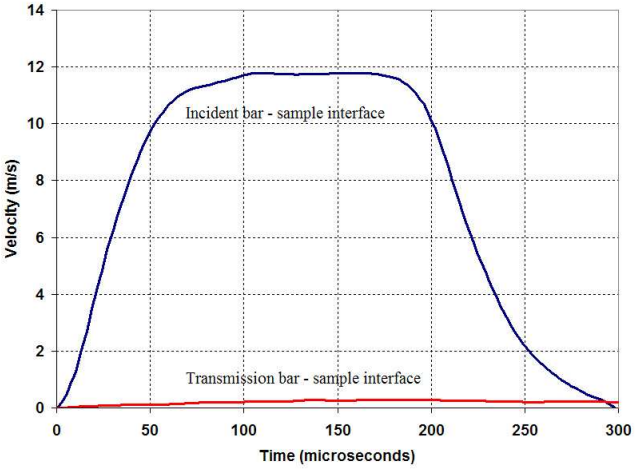

Figure 4. Sample time-resolved velocity profiles acquired during a dynamic tension test.

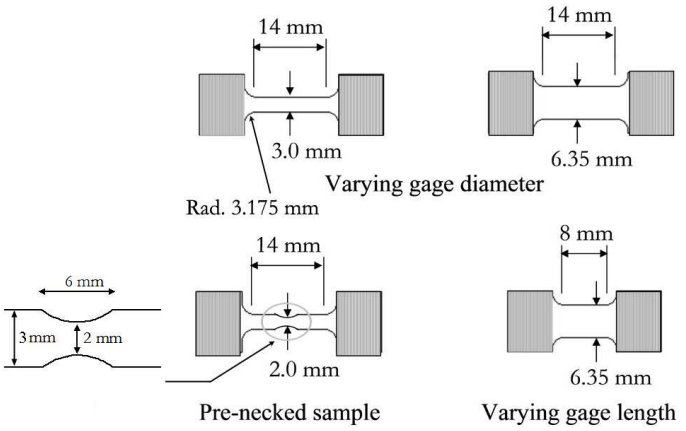

Figure 5. Sample geometries of specimens.

L_g and diameter D_g were machined to help achieve a range of strains and strain rates; see Figure 5. The maximum length L_g was ∼14 mm (overall sample length ∼20 mm).[1] Additionally, prenecks were machined in the gauge section for some specimens to induce locally large deformations without using extremely large loading pulses. Compressive Hopkinson bar tests (strain rate $\sim 4 \times 10^3\ s^{-1}$) of specimens machined axially and transversely from the shipped rod samples showed the material to be fairly isotropic.

2.2. *Numerical simulations.*

2.2.1. *Constitutive model.* The stress-strain behavior of glassy polymers depends strongly on strain rate and temperature, and there exists a transitional threshold depending on strain rate and temperature beyond which the strain rate sensitivity significantly increases. The Ree and Eyring [1955] model for yield captures this transitional behavior using multiple thermally activated processes. Using data over a wide range in temperatures, but at quasistatic strain rates $10^{-4}\ s^{-1}$ to $10^{-1}\ s^{-1}$), Bauwens [1972] related this transition in rate sensitivity to the secondary β viscoelastic transition.

Mulliken and Boyce [2004; 2006] have recently identified and quantitatively characterized this same β transition at very high strain rates. They conducted a comprehensive analytical and experimental study to examine the viscoelastic and viscoplastic behavior of glassy polymers. Dynamic mechanical analysis (DMA) was used to characterize the viscoelastic behavior of PC with focus on rate-dependent shifts of material transitions. These transitions (α, β) are observed to undergo temperature shifts with increasing strain rate, albeit at varying rates. Based upon the DMA test data, Mulliken and Boyce [2006] developed an analytical expression for the elastic modulus by decomposing the storage modulus into its respective α and β components to help predict the elastic behavior over a wide range of strain rates and temperatures, by appropriately shifting the storage modulus to the conditions (temperature and strain rate) at which the material can be expected to undergo a significant change in mechanical behavior.

[1] It takes a minimum of three complete reverberations of the stress wave to attain dynamic equilibrium [Follansbee 1985], implying a duration of approximately 40 μs for this length. In practice, it may take even longer. The true duration must be physically verified by comparing the time-resolved forces on the front and back end [Gray and Blumenthal 2000].

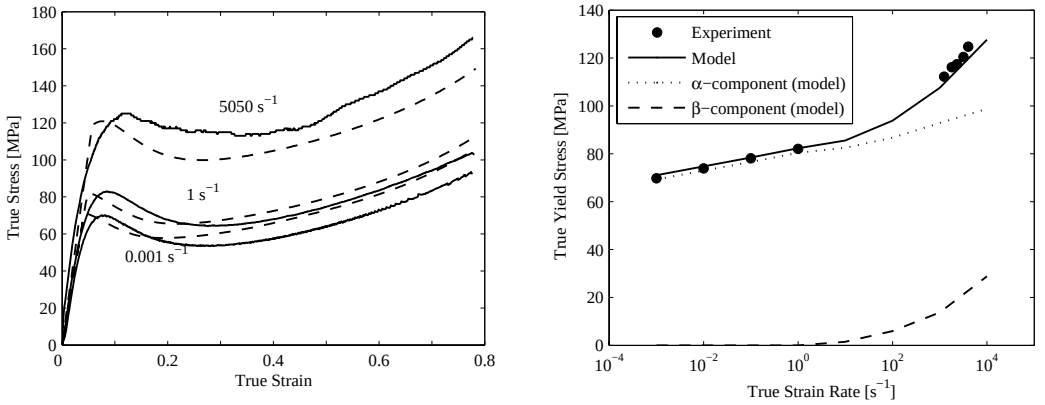

Figure 6. Experimental and model results of the uniaxial compressive stress-strain behavior over a range in strain rates; to the right, yield stress (data and model predictions) as a function of strain rate [Mulliken and Boyce 2006].

Large deformation uniaxial compression tests were conducted on PC under quasistatic and dynamic conditions to determine the rate-dependent yield and post-yield behavior. Figure 6 (left) shows the stress-strain curves for PC for both quasistatic and dynamic compressive tests. The constitutive behavior shows that yield is well defined and followed by strain softening and subsequent strain hardening. Rate sensitivity manifests in the form of increasing yield and flow stress values with increasing strain rate. At right, Figure 6 shows the yield stress plotted against strain rate. The yield stress is seen to increase linearly with strain rate. However, two distinct regions of strain rate sensitivity are observed, indicating a significant material transition in rate sensitivity at $\sim 1.5 \times 10^2\ \mathrm{s}^{-1}$ at room temperature. This insight concerning the strain-rate sensitivity of the viscoelastic transitions was incorporated into a constitutive model by Mulliken and Boyce [2004; 2006].

Constitutive models to describe three-dimensional, temperature and rate dependent, finite-strain deformation of thermoplastic materials have been developed, for example, by Boyce et al. [1988], Arruda and Boyce [1993] and Arruda et al. [1995], and experimentally validated at low to moderate strain rates and

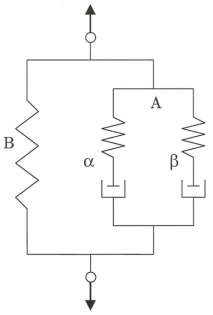

Figure 7. One-dimensional interpretation of the constitutive model [Mulliken and Boyce 2006].

temperatures for a variety of homogeneous and inhomogeneous loading conditions where the strain rates were less than 5 s^{-1}. The rate-dependent three-dimensional constitutive model, developed by Mulliken and Boyce [2006], extends the predictive capabilities to high rates and low temperatures. Figure 7 shows the one-dimensional rheological interpretation of the new model. Segment B is a nonlinear Langevin spring, which represents the molecular network resistance to stretching and alignment. Segment A has two subsegments (α and β) in parallel, each with an elastic spring and viscoplastic dashpot in series. Segment A represents the intermolecular resistance to chain-segment rotation. The two subsegments (α and β) indicate the two distinct thermally activated processes, associated with different molecular-level motions. For PC, the α process relates to the rotation of the polymer main chain and the β process to the local rotations of the main-chain phenyl group. At high temperatures and low strain rates, the contributions due to the β component are minimal and intermolecular resistance is primarily due to the α process. However, at higher rates/lower temperatures, the β process must be activated adding to the intermolecular resistance. The complete three-dimensional, finite-strain kinematical details and material description can be found in [Mulliken and Boyce 2006].

Figure 6 also demonstrates the accuracy of the model in describing the high-rate behavior of PC. At left, it shows the predicted stress-strain curves plotted against the experimentally obtained curves at three different strain rates. At right, it displays the model predictions[2] of yield stress versus strain rate compared to the experimental data. The yield stress values from α and β components are also plotted. The significance of the identification of the contribution made by the β process and its implementation into the constitutive model is evident. The adiabatic conditions at high rates result in significant temperature rise in polymers [Arruda et al. 1995; Garg et al. 2006], which can result in significant post-yield thermal softening; the amount of thermal softening in PC has been found to be modest [Garg et al. 2006] and hence its effect on the stress-strain behavior will be neglected here.

2.2.2. *Stress-strain behavior of PC in tension.* The constitutive response of PC under tension is distinctly different than under compression. Figure 8 shows a comparison of true stress-strain curves obtained using the constitutive model [Mulliken and Boyce 2006] at a range of strain rates (0.001–10,000 s^{-1}) to simulate homogeneous uniaxial compression and tension. The inset in Figure 8 compares the effect of strain rate on the compressive and tensile yield stress. The tensile curves also display rate sensitivity: at the same strain rates, the yield stress values are observed to be lower in tension than in compression, due to pressure sensitivity of yield. Compared to compression, the strain hardening in tension is more dramatic and occurs at lower strains, a result of the strain-induced alignment of polymer chains. In tension, the molecular chains align uniaxially along the axis of elongation, whereas, in compression, the chains align in a plane normal to axis of compression, giving the very different strain hardening behavior.

Depending on the tensile stress-strain behavior of the polymer, tensile loading will produce a homogeneous elongation, a concentrated neck, or a neck that stabilizes and propagates up and down the

[2]As reported in [Sarva et al. 2007], the material parameters for the Mulliken–Boyce constitutive model for Lexan 9034 grade PC manufactured by GE Polymershapes are as follows: the storage modulus as a function of strain rate and temperature, Poisson ratio $\nu_\alpha = \nu_\beta = 0.38$; preexponential factors $\gamma^{\mathrm{p}}_{0,\alpha} = 2.94 \times 10^{16}\,s^{-1}$, $\gamma^{\mathrm{p}}_{0,\beta} = 3.39 \times 10^{5}\,s^{-1}$; activation energies $\Delta G_\alpha = 3.744 \times 10^{-19}$ J, $\Delta G_\beta = 3.769 \times 10^{-20}$ J; softening slope $h_\alpha = 300$ MPa; ratio of steady state to initial intrinsic resistance $s_{\mathrm{ss},\alpha}/s_{0,\alpha} = 0.58$; pressure coefficients $\alpha_{\mathrm{p},\alpha} = 0.168$, $\alpha_{\mathrm{p},\beta} = 0.245$; limiting chain extensibility $\sqrt{N} = 1.52$; rubbery modulus $\mathrm{nk}\theta = 14.2 \times 10^6$ MPa; density $\rho = 1210\,\mathrm{kg\,m^{-3}}$; specific heat $C_p = 1200\,\mathrm{J\,(kg\text{-}K)^{-1}}$; strain rate threshold $\dot{\epsilon}_{th} = 1 \times 10^{-4}\,s^{-1}$.

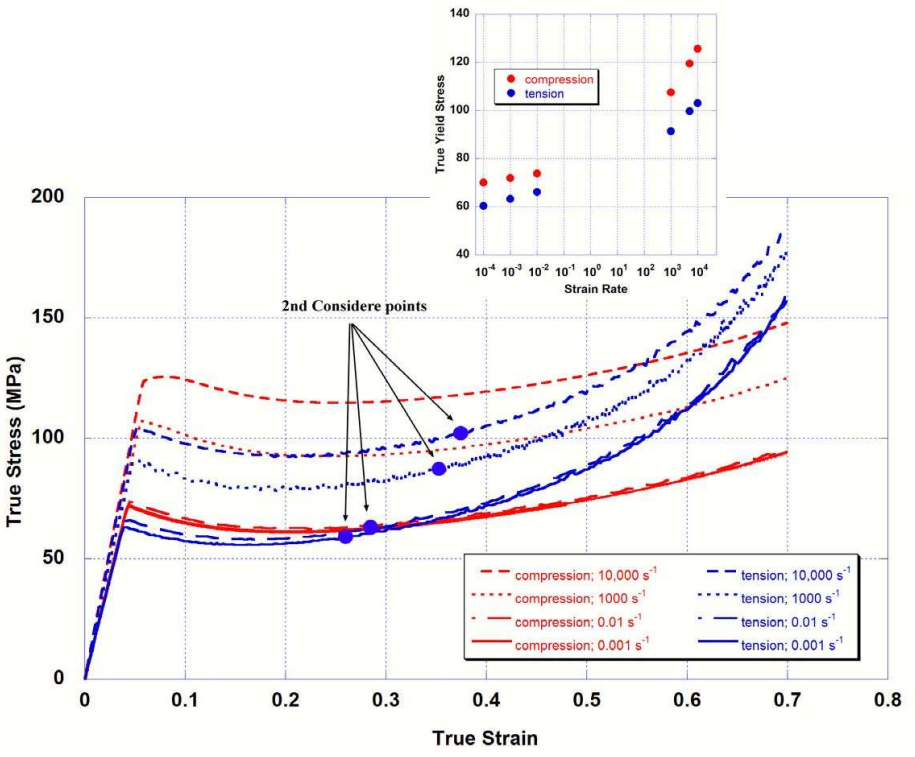

Figure 8. A comparison of the simulated true stress-strain behavior of PC in tension and compression at various strain rates.

specimen length (a process often referred to as cold drawing). A Considère [1885] construction identifies which tensile behavior a material will follow. Following Considère, a neck will initiate when the strain hardening slope fails to overcome the area reduction with tensile strain that occurs at $d\sigma/d\epsilon = \sigma$ (σ = true stress; ϵ = true strain). A neck will stabilize and propagate axially if the strain hardening has increased significantly to compensate for the area reduction as identified by the occurrence of a second Considère point ($d\sigma/d\epsilon = \sigma$) at a later strain. For our case of polycarbonate, the small plateau and/or softening after yield makes the yield point constitute the first Considère point, and a neck will initiate in tension. At larger strains, strain hardening is also significant enough that a second Considère point is found and the neck will stabilize and propagate. The second Considère points for each strain rate are depicted in the stress-strain curves of Figure 8. This necking and cold drawing behavior will be studied further in the experimental data as well as the finite element simulations of the various tensile tests.

2.2.3. *Finite element modeling.* The constitutive model, outlined in Section 2.2.1 and detailed in [Mulliken and Boyce 2006], was implemented into a commercial finite element code, ABAQUS/Explicit, through a user-defined material subroutine. Numerical simulations were conducted to study the deformation behavior of PC samples during quasistatic and dynamic tensile loading. The specimens were modeled as axisymmetric, and 4-node quadrilateral reduced-integration elements (ABAQUS type CAX4) were used. The aluminum Hopkinson bars were not included for simplicity. Experimentally obtained

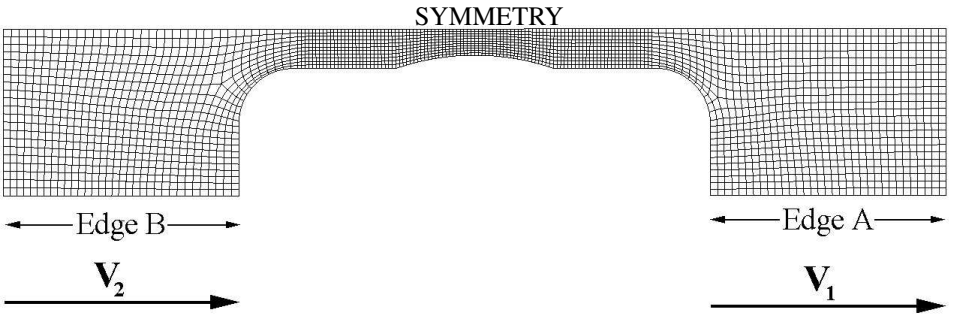

Figure 9. Sample axisymmetric mesh geometry for a precarved neck specimen.

time-resolved velocity profiles of the specimen bar interfaces, similar to those shown in Figure 4, were used as the boundary conditions for the simulations. Figure 9 shows a sample geometry that was used for a precarved neck specimen; a finer mesh was chosen for the gauge section, because the deformation was mostly concentrated in this region. The mesh density was varied from coarse to fine to verify that the chosen mesh provided accurate solutions, and a combined viscous-stiffness form of hourglass control (weight factor = 0.5) was used. No significant variation in results was observed when the viscous-stiffness weight factor was varied from zero (no damping) to one (pure damping). The velocity boundary conditions were applied to the gripping sides (see Edge A and Edge B in Figure 9). Simulations were also performed and studied wherein the boundary conditions were slightly varied (see Appendix A).

3. Results

Tensile tests were conducted for a range of loading conditions. First, for reference and comparison, quasistatic tensile tests were conducted on specimens with uniform diameters at two nominal strain rates. Then, dynamic tension experiments were conducted on a wide array of specimens with varying geometries. The length and diameter were altered and, in some instances, gentle 'precarved neck' regions were specified to vary the extent of inhomogeneity in the resulting deformation progressions. For each geometry, experiments were conducted with increasing striker bar velocity to increase the severity of loading. The experimental results for various cases in the form of nominal stress-strain relationships and photographs of the specimen at various stages of deformation are presented; the nominal stress is calculated as the force divided by the initial cross-sectional area and nominal strain is the increase in specimen length divided by the initial length, taken to be the length of the region with constant cross-sectional area (see Figure 5). Finite element simulations[3] are presented for a few select specimen geometries to detail the mechanics of the deformation progression.

3.1. ***Quasistatic tests.*** As indicated earlier, the stress-strain behavior of PC will result in the classic necking and cold-drawing tensile behavior of polymers (for example and discussion, see [Boyce and

[3]The material parameters for the following FEM simulations were chosen as follows: the limiting chain extensibility is $\sqrt{N} = 1.61$, the pressure coefficients are $\alpha_{p,\alpha} = \alpha_{p,\beta} = 0.105$, and the β-transition shift rate is $\sim 20^{\circ}$C per decade of strain rate. The remaining material parameters are the same as those enumerated in Footnote 2 of Section 2.2.1 and also reported in [Sarva et al. 2007].

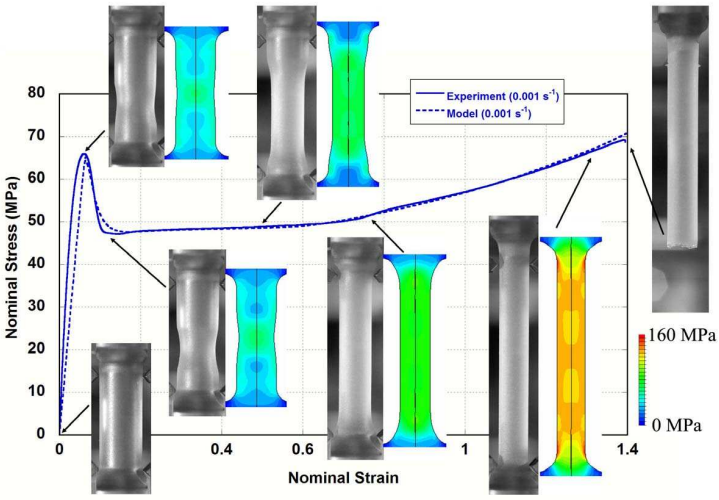

Figure 10. Nominal stress-strain behavior of PC in tension at a nominal strain rate of 0.001 s^{-1}.

Haward 1997]). To review this behavior, quasistatic tensile tests were performed using a Zwick screw driven mechanical tester. Figure 10 shows the nominal tensile stress-strain curve for one such test of a PC specimen ($L_g = 14$ mm, $D_g = 6$ mm) at a nominal strain rate of 0.001 s^{-1}. Photographs of the specimen at various stages of deformation are shown on the figure. The nominal stress-strain curve displays elastic elongation until yield, at which point a neck initiates in the gauge. The neck continues to develop, resulting in a dropping force level (and nominal stress) due to a combination of strain softening in the material and the localized reduction of the specimen cross-sectional area. The neck stabilizes due to the material strain hardening at large strains and axially propagates at near constant force level (and near constant neck diameter). Once the neck has traveled the full gauge length, the force begins to increase significantly due to straining and corresponding strain hardening of the highly strained gauge material. The model-predicted nominal stress-strain curve and the contours of axial stress at various stages of deformation are also shown in Figure 10 for comparison; the model is observed to accurately predict all features of quasistatic tensile behavior.

3.2. *Dynamic tests.*

3.2.1. *Central necking in gauges with small aspect ratio: specimens with 6 mm diameter.* Dynamic tension tests were conducted on specimens with 6 mm diameter and three different lengths: ~ 5 mm, $\sim$8 mm and $\sim$14 mm. Figure 11 shows the nominal stress-strain data; the dotted vertical lines indicate approximately when dynamic equilibrium was achieved in the specimens. In the above data, dynamic equilibrium occurs prior to the initial yielding of the specimen. The varying striker bar velocities and specimen lengths helped achieve a range of strain rates. The increase in the impact velocity of the striker bar also led to an increase in the attained total strain magnitudes. Overall strain rates ranging from $\sim$500 s^{-1} to 900 s^{-1} for the 14 mm length samples, $\sim$1000 s^{-1} to 1400 s^{-1} for the 8 mm length samples, and $\sim$1400 s^{-1} to 1600 s^{-1} for the 5 mm length samples were achieved. Table 1 lists the data (yield stress, strain rate) pairs found for these tests, showing the rate dependence of yield. The initial yield

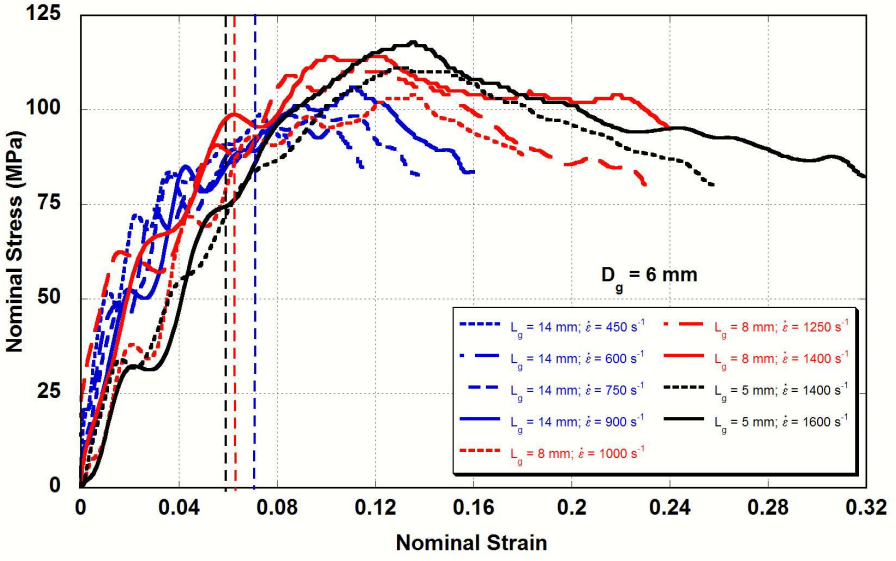

Figure 11. Nominal stress-strain relationships for tests with $D_g = 6\,\text{mm}$, $L_g = 5\,\text{mm}$, 8 mm and 14 mm at the indicated nominal strain rates $\dot{\epsilon}$.

stress is found to range from ∼96 MPa at $600\,\text{s}^{-1}$ to ∼112 MPa at $1600\,\text{s}^{-1}$. After yield, the nominal stress decreases and a neck has initiated.

Figure 12 (top) shows high-speed photographs of an 8 mm length sample captured at various time intervals (90 µs, 200 µs and 300 µs) corresponding to nominal strains of 0.06, 0.18 and 0.27 for the

Gauge Length - L_g (mm)	Nominal (Local) Strain Rate (s^{-1})	Nominal Yield Stress (MPa)
14	600 (1500)	96
14	750 (1875)	97
14	900 (2250)	100
8	1000 (2500)	102
8	1000 (2500)	102.5
8	1250 (3125)	108
8	1400 (3500)	112
5	1400 (3500)	106
5	1400 (3500)	108
5	1600 (4000)	106
5	1600 (4000)	112
5	1600 (4000)	112.5

Table 1. Yield stress at various strain rates for specimens with $D_g = 6\,\text{mm}$.

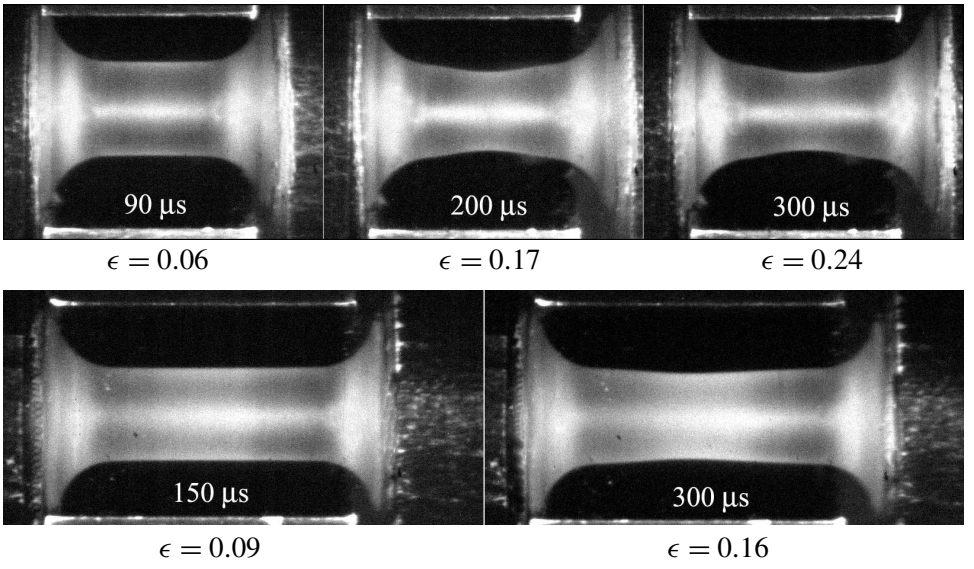

Figure 12. High-speed photographs for tests with $D_g = 6\,\text{mm}$. Above, with $L_g = 8\,\text{mm}$ at a nominal strain rate $\dot{\epsilon} = 1400\,\text{s}^{-1}$, and below, with $L_g = 14\,\text{mm}$ at $\dot{\epsilon} = 900\,\text{s}^{-1}$.

dynamic tension test at $1400\,\text{s}^{-1}$. Until yield, the gauge uniformly elongates. At yield, a neck initiates at the middle whereupon deformation then localizes in the neck. The imposed conditions were not severe enough to fully develop the neck such that neck propagation would occur. Figure 12 (at bottom) shows the high-speed photographs captured during the deformation of a 14 mm length sample at 150 and 300 µs, corresponding to nominal strains of 0.09 and 0.17. The 14 mm length sample also formed a single central neck at the center.

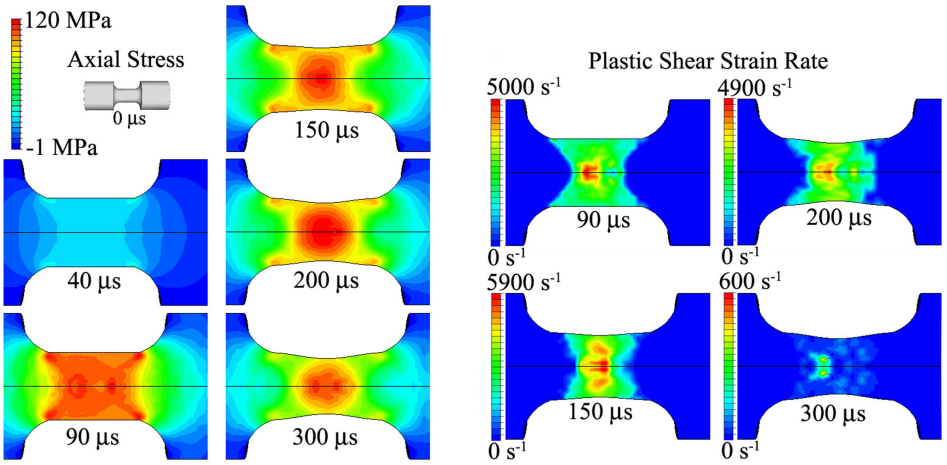

Figure 13. Progression of axial stress (left) and the effective plastic shear strain rate (right) during a test with $D_g = 6\,\text{mm}$ and $L_g = 8\,\text{mm}$ at $\dot{\epsilon} = 1400\,\text{s}^{-1}$.

Simulations were performed to examine the mechanics of high-rate deformation in tension. Figure 13 (left) shows the contours of axial stress at various times during the deformation when $L_g = 8\,\text{mm}$ at $1400\,\text{s}^{-1}$. The intervals were chosen to enable a direct comparison with the high-speed photographs. The displacement initiates from the incident end, resulting in stress fields emanating from that end. After the initial stress wave reverberations, the stress is found to be relatively uniform in the gauge region as shown at 40 μs and 90 μs, which corresponds to elastic deformation. Yielding then occurs at a stress level of 120 MPa and deformation then localizes in a neck at 150 μs; stress levels are then higher in the neck region due to the reduced cross-sectional area. At 300 μs, the stress levels in the neck begin to drop indicating the end of the test. The simulation is seen to replicate the inhomogeneous deformation profile observed in the high-speed photographs accurately.

Figure 13 (right) shows the concurrent evolution of the effective plastic shear strain rate. At 90 μs, the plastic deformation has just initiated and begun to localize in the neck region. By 150 μs the deformation is fully localized in the neck and the local effective plastic shear strain rates reach values greater than $5000\,\text{s}^{-1}$ in some pockets of the necked area. The effective plastic shear strain rate then diminishes as the sample is unloaded.

Figure 14 shows the simulated stress-strain data for a few tests with $L_g = 8\,\text{mm}$ and $L_g = 14\,\text{mm}$. The corresponding experimental results were shown in Figure 11. The nodal reaction force outputs at the two opposite ends were used to calculate the nominal stress-strain relationships. The simulated curves agree favorably with the experimental results and also indicate the ambiguity in clearly identifying the precise yield stress from these tests; the stress levels are similar and also replicated are the features of the yield at ~ 0.1 strain, post-yield decrease in nominal stress, and rate sensitivity.

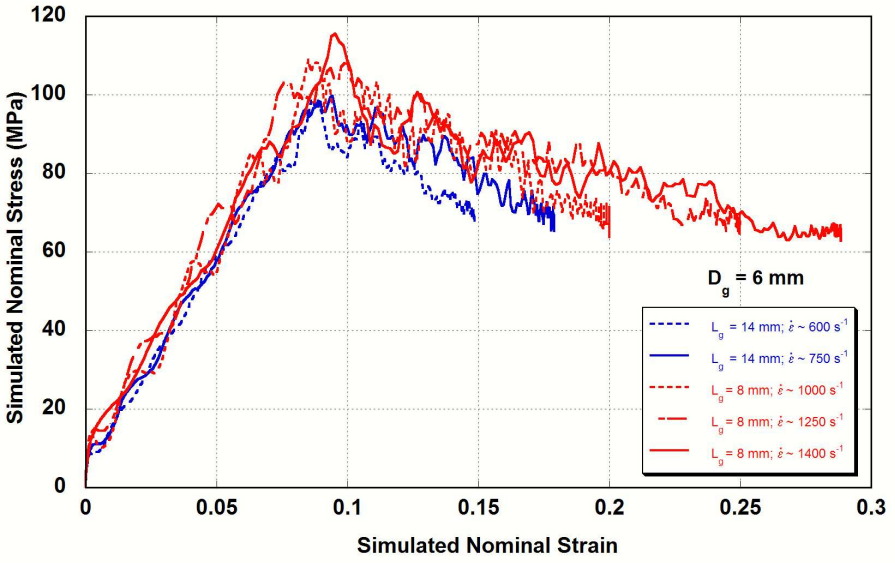

Figure 14. Simulation of stress-strain relationships for a few tests with $D_g = 6\,\text{mm}$, $L_g = 8\,\text{mm}$ and $L_g = 14\,\text{mm}$, shown experimentally in Figure 11.

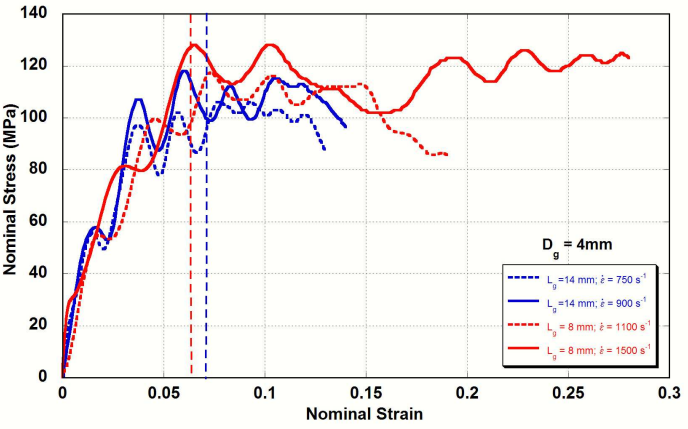

Figure 15. Nominal stress-strain relationships for tests with $D_g = 4$ mm and $L_g = 8$ mm and 14 mm.

3.2.2. *Transition to double necking in gauges with large aspect ratio: specimens with 4 mm diameter.* Samples with diameter of 4 mm were tested to examine the effects of aspect (L/D) ratio on the mechanics of necking during dynamic loading conditions. Figure 15 shows the nominal stress-strain data for the 8 mm and 14 mm length samples. The strains and strain rates attained are similar to those observed for the corresponding 6 mm diameter samples. Yield strains for these specimens are again observed to be in the ~ 0.1 range (similar to those observed in Figure 11).

Figure 16 shows high-speed photographs for tests with $L_g = 8$ mm and 14 mm. For the 8 mm length sample, elongation causes a single distinctive neck to form at the center. However, the bottom group shows that when the sample length is increased to 14 mm, the deformation mode undergoes a transition. The frame at 150 µs shows no necking. Further elongation leads to nearly simultaneous initiation of two distinct necks located equidistant from the center; see the frame at 225 µs. Each neck further develops as seen in the frame at 280 µs. This double necking has also been observed in metals by other researchers [Wood 1967; Rusinek et al. 2005] and is attributed to wave propagation during dynamic tensile elongation.

3.2.3. *Specimens with 3 mm diameter.* To further examine the phenomenon of multiple necking, samples were machined with even greater L/D ratio ($D_g = 3$ mm; $L_g = 8$ mm and 14 mm). The samples were tested, and Figure 17 shows the nominal stress-strain relationships. Overall nominal strain rates in the range of 800 s^{-1} and 1600 s^{-1} were achieved. Nominal stress levels well above 100 MPa are observed.

The top of Figure 18 shows high-speed photographs of the specimen with $L_g = 8$ mm at 1600 s^{-1} at various time intervals corresponding to nominal strains of 0.07, 0.21 and 0.3. The bottom of Figure 18 shows the silhouette photographs captured through the window in the collar for a test on a 14 mm length sample at 800 s^{-1} at various time intervals, corresponding to nominal strains of 0.08, 0.12 and 0.15. Similar to the 4 mm diameter samples, these show a single neck formation for the 8 mm length specimen and a double neck formation for the 14 mm length specimen. The loading conditions are such that the double necks become more fully developed for this 3 mm diameter case than those observed

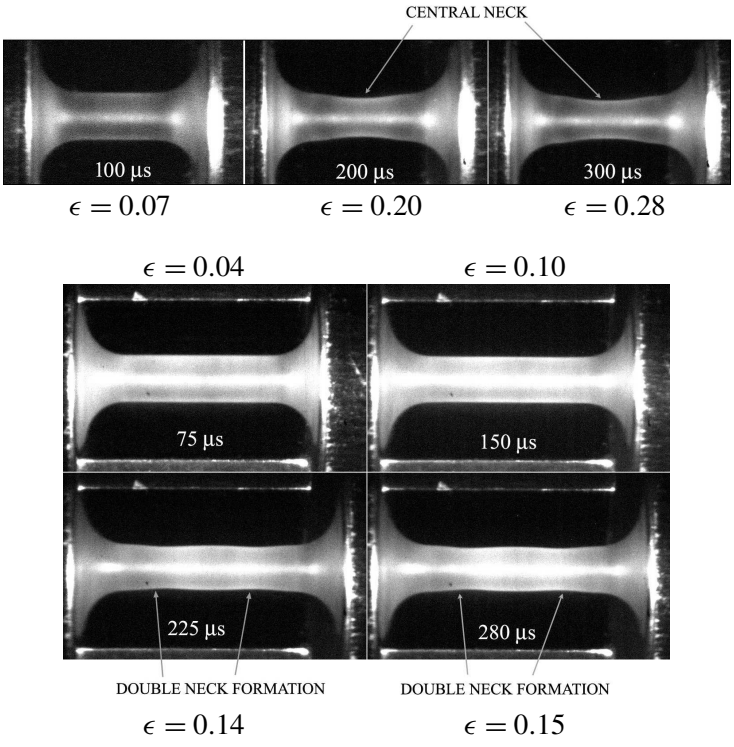

Figure 16. High-speed photographs for tests with $D_g = 4$ mm. At top, $L_g = 8$ mm and $\dot{\epsilon} = 1500\,\mathrm{s}^{-1}$. At bottom, $L_g = 14$ mm and $\dot{\epsilon} = 900\,\mathrm{s}^{-1}$.

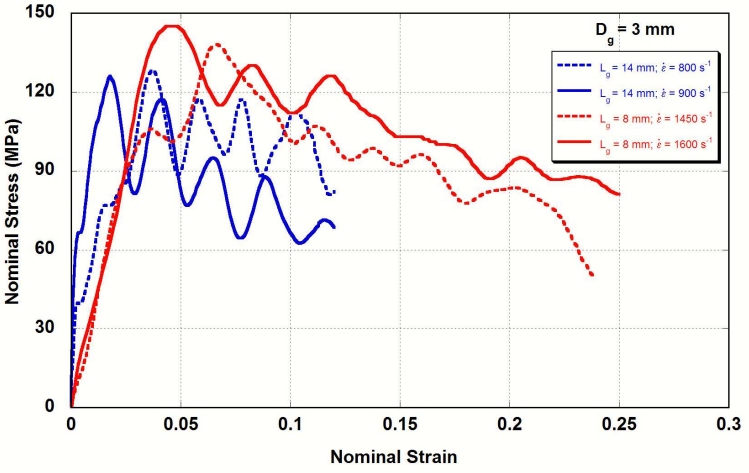

Figure 17. Nominal stress-strain relationships for tests with $D_g = 3$ mm and $L_g = 8$ mm and 14 mm.

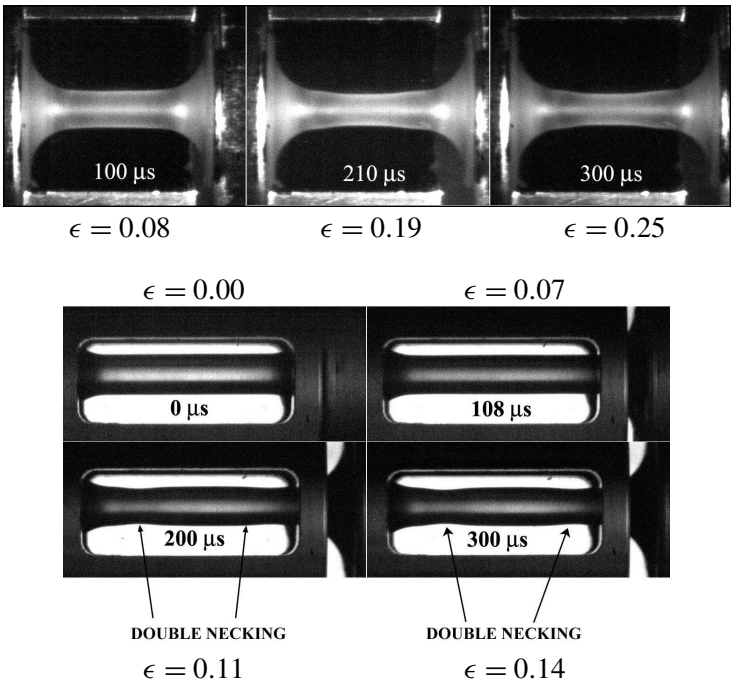

Figure 18. High-speed photographs for tests with $D_g = 3\,\text{mm}$. At top, with $L_g = 8\,\text{mm}$ at $\dot{\epsilon} = 1600\,\text{s}^{-1}$. At bottom, with $L_g = 14\,\text{mm}$ at $\dot{\epsilon} = 800\,\text{s}^{-1}$.

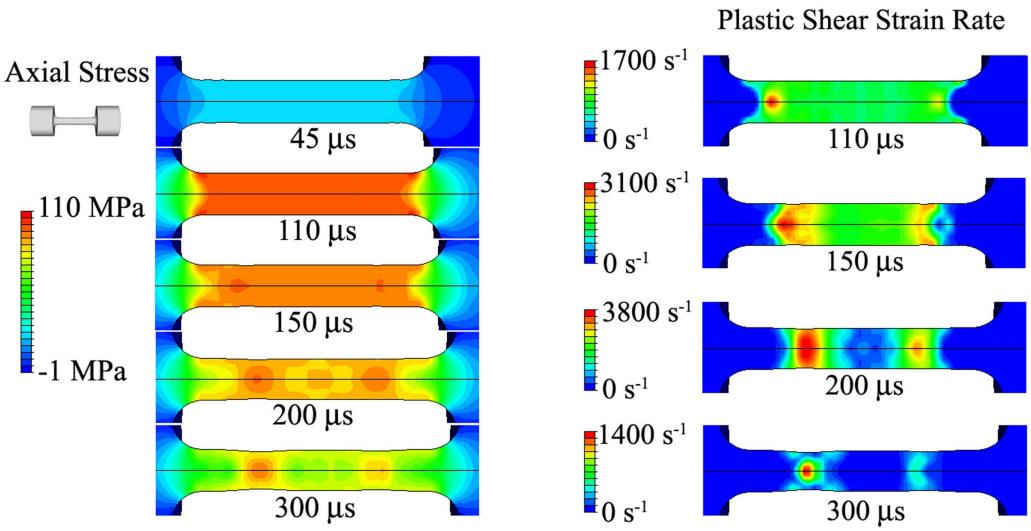

Figure 19. Progression of axial stress (left) and the effective plastic shear strain rate (right) during a test with $D_g = 3\,\text{mm}$ and $L_g = 14\,\text{mm}$ at $\dot{\epsilon} = 800\,\text{s}^{-1}$.

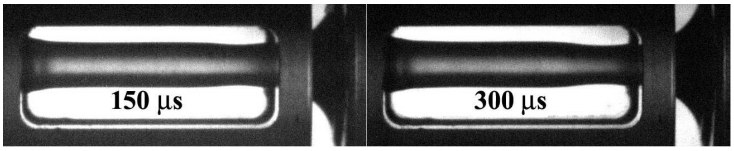

Figure 20. High-speed photographs for tests with $D_g = 3\,\text{mm}$ and $L_g = 14\,\text{mm}$ at $\dot{\epsilon} = 900\,\text{s}^{-1}$.

earlier in the 4 mm diameter case (of the same length). At greater overall elongation, the left neck is observed to become dominant.

Simulations were performed to examine the double necking phenomenon. Figure 19 (left and right) shows the contours of axial stress and effective plastic shear strain rate, respectively, during a test with $D_g = 3\,\text{mm}$ and $L_g = 14\,\text{mm}$ at $800\,\text{s}^{-1}$. The contours show uniform deformation until reaching initial yield whereupon two necks initiate equidistant from the two ends. The second neck is seen to initiate within a few microseconds after the first neck initiates. As the deformation continues, the left neck begins to dominate.

3.2.4. *The effect of loading velocity.* The striker bar velocity and hence the strain rate were further increased for samples with D = 3 mm and $L_g = 14\,\text{mm}$. Figure 20 shows the high speed photographs for such a test at a strain rate of $900\,\text{s}^{-1}$. Interestingly, as the loading velocity is further increased, the deformation mode changes to the formation of a single deep neck towards the incident/loading end; these observations were repeated for two tests performed under the same conditions. For slender gauges, the number of necks formed, their location, and which one becomes dominant are dependent on the elongation velocity and the boundary conditions (see Appendix A for a brief discussion of the gripping mechanism). The single neck formation at one end seen in Figure 20 has also been observed by Wood [1967] during tests on metals at higher elongation rates.

3.2.5. *Drawing of neck in gauges with locally reduced cross section: specimens with 3 mm diameter and a 2 mm diameter precarved neck.* SHTBs typically have limitations in the total displacement that can be attained during a test; the experimental limit was $\sim 3\,\text{mm}$ in the present equipment. Hence, a reduced diameter region (to be referred to as 'precarved neck') was precarved/machined in the gauge section to

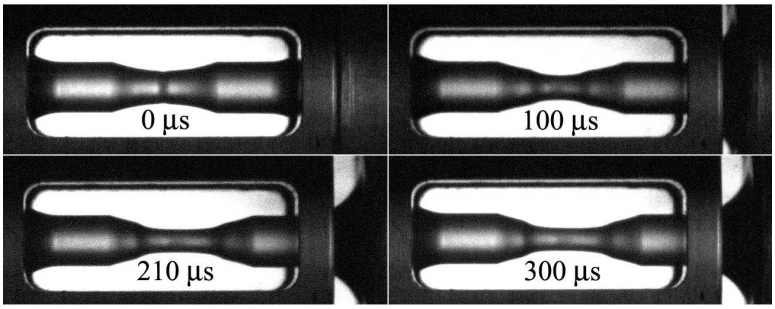

Figure 21. High-speed photographs obtained during a test with $D_g = 3\,\text{mm}$, $L_g = 14\,\text{mm}$ and precarved neck diameter of 2 mm at an elongation rate of $9\,\text{ms}^{-1}$.

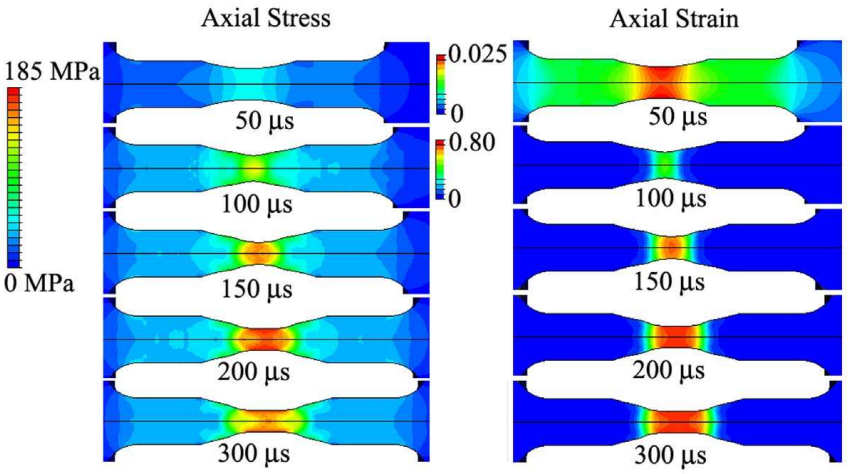

Figure 22. Progression of axial stress (left) and axial strain (right) during a test with $D_g = 3$ mm, $L_g = 14$ mm, and a precarved neck diameter of 2 mm.

enhance the local strain level so that it reaches a region of the stress-strain curve that exhibits significant strain hardening (recall Figure 8), enabling the neck to stabilize and axially propagate. Figure 21 depicts the high-speed photographs obtained during a test on a sample with a precarved neck ($D_g \sim 3$ mm; $L_g \sim 14$ mm; precarved neck diameter ~ 2 mm). The deformation initially localizes in the precarved neck. As the necked region axially strains, the material strain hardening stabilizes the neck and the neck propagates. Since the precarved neck geometry is tapered (as opposed to being of initially uniform diameter), the location that first yields and further necks will continue to axially strain (and experience ongoing reduction in diameter) as the neck also axially propagates.

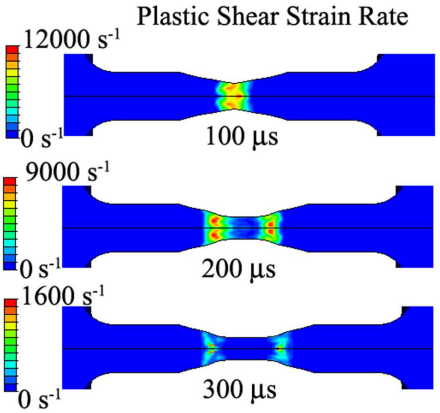

Figure 23. Contours of effective plastic shear strain rate at shown intervals during a test with $D_g = 3$ mm, $L_g = 14$ mm and precarved neck diameter of 2 mm.

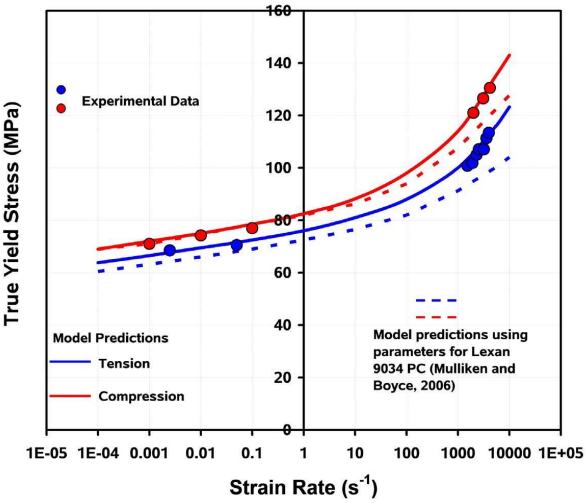

Figure 24. Comparison of the experimentally observed compressive and tensile yield stress values at various strain rates and the corresponding model predictions.

Simulations of the dynamic loading of the precarved specimen were found to successfully predict the details of the observed progression of deformation. Figure 22 shows the evolution of axial stress and axial strain contours during the test. The simulation is found to replicate the experimentally observed deformation profiles of Figure 21. Figure 23 shows the evolution of the effective plastic shear strain rate. The locally reduced cross-section of the precarved region has helped accomplish much greater local effective plastic shear strain rates than in samples with the larger uniform diameters. Effective plastic shear strain rates as high as $10000\,\mathrm{s}^{-1}$ are observed during the initial stages of plastic deformation. As the test progresses, the active plastic deformation rates are highest in the shoulder regions adjacent to the plastically developed neck, signifying axial propagation of the neck, that is, a cold drawing process.

4. Discussion

Figure 24 shows a comparison of the experimentally observed true yield stress values in compression[4] and tension for the investigated PC and the corresponding model predictions. As expected, the yield stress values display an increased rate sensitivity at high rates in both compression and tension, and the yield stress values in tension are slightly lower than the corresponding values in compression at similar strain rates, due to the pressure sensitivity of yield. Note that the inhomogeneous nature of the initial yield during tension results in a locally higher strain rate at yield when compared to the nominal rate; through simulations we have determined this amplification to be by a factor of approximately 2.5.

Although some studies have been conducted to examine the effects of loading velocity on the necking in tensile metallic specimens, the phenomenon of dynamic necking in polymers has been largely unexplored. The earliest systematic experiments on dynamic necking were performed by Wood [1967] using tensile specimens made of various steels and alloys. He observed that as the extension rate is

[4]The high rate compression tests were performed on a compressive SHPB at MIT.

Aspect ratio	Gauge Dia.	Gauge Length	Strain Rate (Nominal)	Necking Mode
0.83	6 mm	5 mm	1400–1600 s^{-1}	single central neck
1.33	6 mm	8 mm	1000–1400 s^{-1}	single central neck
2.33	6 mm	14 mm	450–900 s^{-1}	single central neck
2.00	4 mm	8 mm	1300–1500 s^{-1}	single central neck
2.66	3 mm	8 mm	1450–1600 s^{-1}	single central neck
3.50	4 mm	14 mm	600–900 s^{-1}	double necking
4.66	3 mm	14 mm	600–800 s^{-1}	double necking, neck opposite to loading side grows dominant
4.66	3 mm	14 mm	900 s^{-1}	single neck, neck forms close to loading side

Table 2. A list of necking patterns for various test geometries and strain rates.

increased, the ductility of the material (defined as strain at failure) initially increases, then plateaus at higher velocities, and finally rapidly diminishes upon reaching a critical velocity. Correspondingly, the mode of necking changes from formation of a neck anywhere along the gauge section at static loading rates, to formation of a neck close to the fixed side as the velocity is increased, to the formation of symmetric double necks with fracture occurring at either neck, to formation of double necks with fracture occurring close to the loading end, and finally to induction of a single neck with fracture occurring close to the loading end.

Table 2 enumerates the inhomogeneous deformation modes for various test geometries and strain rates observed in the present study. For samples where the aspect ratio of the gauge section is less than three, the dynamic extension results in a single neck formation in the middle for strain rates up to 1600 s^{-1}. As the gauge is made more slender and the aspect ratio is increased (beyond three), the deformation mode changes to an almost simultaneous formation of two necks equidistant from the center. Note that a sample with $L_g = 14$ mm and $D_g = 6$ mm (Figure 12, bottom) shows a single neck, whereas samples with the same length but with 4 mm and 3 mm diameter show double necking (Figures 16, bottom, and 18, bottom). In the sample with $L_g = 14$ mm and $D_g = 3$ mm, which was tested at a strain rate of 800 s^{-1}, it is observed that with elongation, the neck opposite to the incident end grows dominant. When the strain rate was further increased for this geometry (to 900 s^{-1}), the necking mode then changed to formation of a single neck close to the incident end. These complex necking patterns arise from the wave propagation characteristics and the resulting interactions that depend on the specimen geometry and loading rate. The above test results do not span the gamut of necking modes recorded by Wood [1967], but the observed transitions are consistent with his experimental results on metals.

Along with the effects of geometry and rate, the stress-strain behavior of the material will strongly govern the necking behavior observed during dynamic tensile loading. Here, finite element simulations were conducted to examine the effects of stress-strain behavior on specimen deformation, while density and boundary conditions were kept the same. The material parameters in the model [Mulliken and Boyce 2006] were varied to obtain five different stress-strain behaviors as depicted in Figure 25 for a

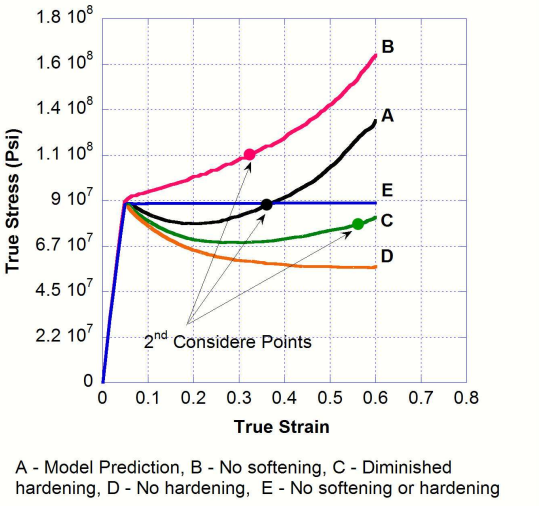

Figure 25. Comparison of five different cases of stress-strain behavior under uniaxial tension at $\dot{\epsilon} = 1000\,\mathrm{s}^{-1}$.

strain rate of $1000\,\mathrm{s}^{-1}$ (the rate sensitivity of yield is identical for each case; it is the post-yield behavior that is varied as shown). Curve A shows the model prediction of the actual PC material. In curve B, post-yield strain softening has been suppressed and strain hardening begins immediately after yield; however, at these strain rates, the stress levels are such that this level of strain hardening does not suppress neck initiation (that is, this constitutive response does exhibit a first Considère point and also a second stabilizing Considère point). In curve C, the strain softening has been maintained and the strain hardening has been reduced, resulting in the second Considère point occurring at a much later strain. In curve D, the hardening has been completely eliminated, resulting in the extreme strain softening and no second Considère point. Finally, in curve E, both softening and hardening have been suppressed, resulting in constant stress levels after rate dependent yield and no second Considère point. Here, the effects of these five stress-strain behaviors on the neck initiation phenomenon during dynamic tensile loading of a high aspect ratio bar ($L_g = 14\,\mathrm{mm}$ and $D_g = 3\,\mathrm{mm}$) at a nominal strain rate of $800\,\mathrm{s}^{-1}$ are studied and the effects of these stress-strain behaviors on the deformation of the precarved neck case (and corresponding neck evolution with large strains) are also studied.

Figure 26 (left) shows the effect of constitutive behavior on the deformation of the high aspect ratio bar ($L_g = 14\,\mathrm{mm}$ and $D_g = 3\,\mathrm{mm}$) at a nominal strain rate of $800\,\mathrm{s}^{-1}$. Contours of chain stretch[5] (λ_{chain}) are plotted at 300 μs for each case. Case A shows the model prediction of the actual PC experiment which captures the observed behavior. For case B, a very gentle neck is initiated and the axial deformation is spread over a greater length of the specimen, significantly reducing the maximum induced stretch levels; this behavior is attributed to the strain hardening that ensues immediately after yield which tends to begin to stabilize and spread the deformation soon after initial yield. In case C, it is observed that the greater

[5]Stretch on a chain in an eight-chain network $\lambda_{\mathrm{chain}} = \sqrt{\mathrm{trace}(\overline{\mathbf{B}}_{\mathrm{B}})/3}$, where $\overline{\mathbf{B}}_{\mathrm{B}} = (\det \mathbf{F})^{-2/3}\mathbf{F}\mathbf{F}^{\mathrm{T}}$ and $\mathbf{F}$ is the deformation gradient.

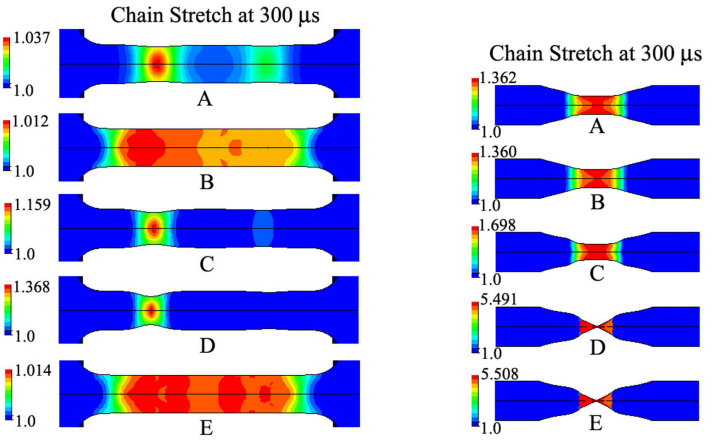

Figure 26. Left: effect of constitutive behavior on the necking for a test with $D_g = 3$ mm, $L_g = 14$ mm at $\dot{\epsilon} = 800\,\mathrm{s}^{-1}$. Right: with $D_g = 3$ mm, $L_g = 14$ mm and precarved neck diameter = 2 mm at $\dot{\epsilon} = 9\,\mathrm{ms}^{-1}$.

strain softening and delayed strain hardening results in the double neck formation where the deformation is found to be more localized with even more prominent neck formation than the reference case A. In case D, where the hardening has been eliminated, the localization is extreme and one neck is greatly dominant. For case E, a single neck initiates, albeit in a more gentle manner than those cases with strain softening, demonstrating as expected the role of strain softening in highly localizing the deformation.

Figure 26 (right) shows the effect of constitutive behavior on the deformation of a 3 mm diameter sample with a 2 mm precarved neck. Case A shows the model prediction which captures the experimentally observed drawing of the neck. Case B, in which the softening has been suppressed, shows the deformation profile to be similar due to the presence of the initial precarved neck region (where the precarved neck aids in creating the initial local neck—this material exhibits a relatively weak first Considère point in its inherent behavior); the post-yield strain hardening then axially propagates the deformation. Case C exhibits a greater stretching of the necked region prior to axial propagation of the neck (cold drawing) due to the second Considère point occurring at a larger axial strain. In case D, in which the hardening is eliminated, the deformation fully localizes in a neck which never stabilizes (no second Considère point) as expected; note that failure was not incorporated in the model. In case E, in which both softening and hardening are removed, the deformation also fully localizes in an unstable neck, as expected.

5. Summary

Polymers are extensively used in applications where they are routinely subjected to deformations at large strain rates, but very few studies of the dynamic tensile behavior of polymers have been conducted due to the intricate nature of the experimental techniques as well as the difficulty in capturing the subtleties of the constitutive stress-strain behavior in simulations. Yet, it is essential that polymers are tested under dynamic tension for a complete evaluation of their high-rate constitutive behavior and also for studying the progression of such typically inhomogeneous deformations. In this study, a comprehensive experimental and finite element study of polycarbonate was conducted to examine the mechanics of inhomogeneous

deformations over wide ranging conditions of high-rate tension. A range of test conditions was achieved by varying the loading velocity and modifying the specimen geometry. The high-rate tensile yield behavior was quantified at nominal strain rates of 500–1500 s^{-1} and compared with the quasistatic tensile behavior. Depending on the aspect ratio and the cross sectional area, deformation modes ranging from single necking to double necking to drawing of the neck were observed. For each case, the progression of deformation was recorded through high speed photography and the mechanics were examined using finite element simulations along with a three-dimensional elastic-viscoplastic constitutive model for the high-rate behavior of glassy polymers. The model accurately predicted the deformation profiles for the entire spectrum of test conditions. The changes in necking behavior of polymers under dynamic tension had hitherto not been characterized. At high rates, in addition to the material stress-strain behavior and its rate sensitivity, the inhomogeneous deformation modes were seen to be governed by wave propagation effects and the ensuing interaction with specimen geometry. A parametric finite element study was also performed to examine the effects of stress-strain behavior on the necking mode. These observations also indicated that it is critical that the constitutive model accurately predict all features of the stress-strain behavior to capture the overall inhomogeneous deformations. This study accomplishes a quantitative study of tensile yield stress of polycarbonate, characterizes the necking modes for a multitude of test conditions, unravels the mechanics of tensile elongation, and validates a high-rate constitutive model for a range of inhomogeneous deformations.

Appendix A. The effects of boundary conditions

Ideally, it is preferred that the gripping method have very little bearing on the tensile deformation of the specimen, but it is often observed to affect the dynamic deformation patterns. In a gripping technique such as that used in the present study (threaded ends), one has to pay careful attention to the consistency in the machining of these ends, since small variations in the threading dimensions can lead to changes in the gripping mode. To examine the effects of such variations, numerical simulations were performed with slightly altered boundary conditions.

Figure 27 compares three such variations in boundary conditions. In case A, the grip region perimeter is restrained in the radial direction and the velocity profiles are applied to these sides to model a tightly threaded sample. The simulated deformation profile displays double necking, in which the right neck is more dominant. In case B, the perimeter is still radially restrained, but the velocity profiles are applied only to the opposing parallel faces and not to the entire sides. This results in a deformation mode change such that a greatly dominant neck is formed to the left. In the third case, the boundary conditions are changed so that the perimeter is no longer radially constrained, and the velocity profiles are applied to grip region as shown. These conditions represent a scenario in which the sample is loosely threaded in the bars, allowing for radial movement of the dog-bone ends. For this case, the simulation matches the experimentally observed double necking seen in the high speed photographs (Figure 18, bottom), wherein the left neck is more dominant. These results clearly demonstrate the susceptibility of the deformation mode to the gripping method and the need for careful consideration of such factors when analyzing the dynamic deformations.

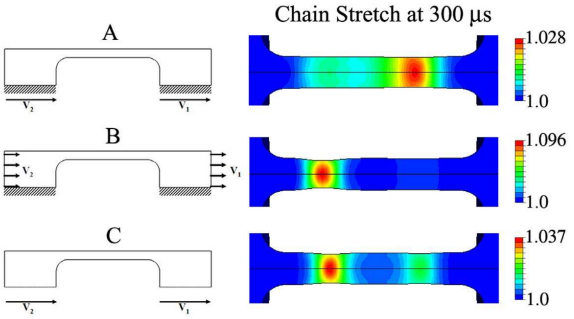

Figure 27. Effect of boundary conditions on the deformation of a sample with $D_g = 3\,\text{mm}$, $L_g = 14\,\text{mm}$ at $\dot{\epsilon} = 800\,\text{s}^{-1}$; contours of chain stretch at 300 μs are plotted.

Appendix B. The effect of variation in density

Similarly, simulations were performed to examine the effects of variations in the material density. The density was varied at intervals from $0.1\,\rho_{\text{PC}}$ to $2\,\rho_{\text{PC}}$ ($\rho_{\text{PC}} = 1.21\,\text{g/cm}^3$), while the remaining material parameters were unchanged. The deformation modes were seen to vary significantly as the density was varied (see Figure 28). As the material density increased, simulations showed a marked reduction in the wave propagation speed (note that the longitudinal elastic wave speed $C_e \sim \sqrt{\text{E}/\rho}$; E = Elastic Modulus), slowing the deformation process. The resulting necking pattern then depended on how the wave propagates within the specific specimen geometry. These results show the manner in which any mass inertia effects during the dynamic loading may affect the wave propagation, ultimately affecting the overall deformation.

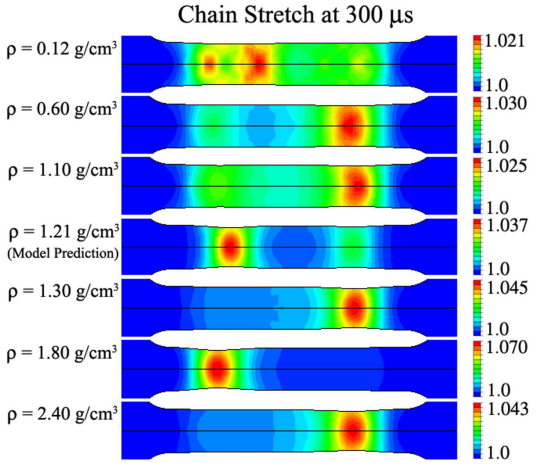

Figure 28. Effect of density on the deformation of a sample with $D_g = 3\,\text{mm}$, $L_g = 14\,\text{mm}$ at $\dot{\epsilon} = 800\,\text{s}^{-1}$; contours of chain stretch at 300 μs are plotted.

Acknowledgements

The authors thank Adam D. Mulliken for providing the user subroutine for the constitutive model and Mohit Garg and Sharon Y. Soong for their assistance during the experiments.

References

[Argon 1973] A. S. Argon, "A theory for the low-temperature plastic deformation of glassy polymers", *Philos. Mag.* **28**:4 (1973), 839–865.

[Arruda and Boyce 1993] E. M. Arruda and M. C. Boyce, "Evolution of plastic anisotropy in amorphous polymers during finite straining", *Int. J. Plasticity* **9**:6 (1993), 697–720.

[Arruda et al. 1995] E. M. Arruda, M. C. Boyce, and R. Jayachandran, "Effects of strain rate, temperature and thermomechanical coupling on the finite strain deformation of glassy polymers", *Mech. Mater.* **19**:2-3 (1995), 193–212.

[Bauwens 1972] J. C. Bauwens, "Relation between the compression yield stress and the mechanical loss peak of bisphenol-A-polycarbonate in the β transition range", *J. Mater. Sci.* **7**:5 (1972), 577–584.

[Boyce and Haward 1997] M. C. Boyce and R. N. Haward, "The post yield deformation of glassy polymers", pp. 213–293 in *The physics of glassy polymers*, edited by R. N. Haward and R. Young, Chapman and Hall, London, 1997.

[Boyce et al. 1988] M. C. Boyce, D. A. Parks, and A. S. Argon, "Large inelastic deformation of glassy polymers. part I: Rate dependent constitutive model", *Mech. Mater.* **7**:1 (1988), 15–33.

[Caddell and Kim 1981] R. M. Caddell and J. W. Kim, "Influence of hydrostatic pressure on the yield strength of anisotropic polycarbonate", *Int. J. Mech. Sci.* **23**:2 (1981), 99–104.

[Chen et al. 1999] W. Chen, B. Zhang, and M. J. Forrestal, "A split-Hopkinson bar technique for low-impedance materials", *Exp. Mech.* **39**:2 (1999), 81–85.

[Chen et al. 2000] W. Chen, F. Lu, and B. Zhou, "A quartz-crystal-embedded split Hopkinson pressure bar for soft materials", *Exp. Mech.* **40** (2000), 1–6.

[Chen et al. 2002] W. Chen, F. Lu, and M. Cheng, "Tension and compression tests of two polymers under quasi-static and dynamic loading", *Polym. Test.* **21**:2 (2002), 113–121.

[Cheng and Chen 2003] M. Cheng and W. Chen, "Experimental investigation of the stress-stretch behavior of EPDM rubber with loading rate effects", *Int. J. Solids Struct.* **40**:18 (2003), 4749–4768.

[Considère 1885] A. G. Considère, "Mémoire sur l'emploi du fer et de l'acier dans les constructions", *Annales des Ponts et Chausses* (*ser. 6*) **9** (1885), 574–775.

[Field et al. 2004] J. E. Field, S. M. Walley, W. G. Proud, H. T. Goldrein, and C. R. Siviour, "Review of experimental techniques for high rate deformation and shock studies", *Int. J. Impact Eng.* **30**:7 (2004), 725–775.

[Follansbee 1985] P. S. Follansbee, *The* H*opkinson bar*, vol. 8, 9th ed., American Society for Metals, Metals Park, OH, 1985.

[Garg et al. 2006] M. Garg, A. D. Mulliken, and M. C. Boyce, "Temperature rise in polymeric materials during high rate deformation", *J. Appl. Mech.* (2006). Accepted for publication.

[Gray 2000] G. T. Gray, *Classic split-*H*opkinson pressure bar testing*, vol. 8, 10th ed., ASM International, Materials Park, OH, 2000.

[Gray and Blumenthal 2000] G. T. Gray and W. R. Blumenthal, *Split-*H*opkinson pressure bar testing of soft materials*, vol. 8, 10th ed., ASM International, Materials Park, OH, 2000.

[Gray et al. 1997] G. T. Gray, W. R. Blumenthal, C. P. Trujillo, and R. W. Carpenter, "Influence of temperature and strain rate on the mechanical behavior of adiprene L-100", *Journal de Physique* (*France*) *IV Colloqium, C3* (*EURODYMAT 97*) **7** (1997), 523–528.

[Gray et al. 1998] G. T. Gray, C. M. Cady, and W. R. Blumenthal, "Influence of temperature and strain rate on the constitutive behavior of Teflon and Nylon", pp. 955–958 in *Plasticity 99: constitutive and damage modeling of inelastic deformation and phase transformation*, edited by A. S. Kahn, Neat Press, Fulton, MD, 1998.

[Harding et al. 1960] J. Harding, E. O. Wood, and J. D. Campbell, "Tensile testing of materials at impact rates of strain", *J. Mech. Eng. Sci.* **2** (1960), 88–96.

[Kolsky 1963] H. Kolsky, *Stress waves in solids*, Dover, New York, 1963.

[Lindholm and Yeakley 1968] U. S. Lindholm and L. M. Yeakley, "High strain-rate testing: tension and compression", *Exp. Mech.* **8**:1 (1968), 1–9.

[Moy et al. 2003] P. Moy, T. Weerasooriya, A. Hsieh, and W. Chen, "Strain rate response of a poly-carbonate under uniaxial compression", pp. 269–275 in *Proceedings of the SEM Annual Conference on Experimental and Applied Mechanics* (Charlotte, NC), 2003.

[Mulliken and Boyce 2004] A. D. Mulliken and M. C. Boyce, "Low to high strain rate deformation of amorphous polymers", pp. Paper No. 197 in *Proceedings of the 2004 SEM X International Congress and Exposition on Experimental and Applied Mechanics*, Costa Mesa, CA, 2004.

[Mulliken and Boyce 2006] A. D. Mulliken and M. C. Boyce, "Mechanics of rate-dependent elastic-plastic deformation of glassy polymers from low to high strain rates", *Int. J. Solids Struct.* **43**:5 (2006), 1331–1356.

[Nicholas 1981] T. Nicholas, "Tensile testing of materials at high rates of strain", *Exp. Mech.* **21**:5 (1981), 177–185.

[Rae and Brown 2005] P. J. Rae and E. N. Brown, "The properties of poly(tetrafluoroethylene) (PTFE) in tension", *Polymer* **46**:19 (2005), 8128–8140.

[Ree and Eyring 1955] T. Ree and H. Eyring, "Theory for non-newtonian flow I. Solid plastic system", *J. Appl. Phys.* **26**:7 (1955), 793–800.

[Richeton et al. 2006] J. Richeton, S. Ahzi, K. S. Vecchio, F. C. Jiang, and R. R. Adharapurapu, "Influence of temperature and strain rate on the mechanical behavior of three amorphous polymers: Characterization and modeling of the compressive yield stress", *Int. J. Solids Struct.* **43**:7-8 (2006), 2318–2335.

[Rusinek et al. 2005] A. Rusinek, R. Zaera, J. R. Klepaczko, and R. Cheriguene, "Analysis of inertia and scale effects on dynamic neck formation during tension of sheet steel", *Acta Mater.* **53**:20 (2005), 5387–5400.

[Sarva et al. 2007] S. Sarva, A. D. Mulliken, and M. C. Boyce, "Mechanics of Taylor impact testing of polycarbonate", *Int. J. Solids Struct.* **44**:7-8 (2007), 2381–2400.

[Sawas et al. 1998] O. Sawas, N. S. Brar, and R. A. Brockman, "Dynamic characterization of compliant materials using an all-polymeric split Hopkinson bar", *Exp. Mech.* **38**:3 (1998), 204–210.

[Sivior et al. 2005] C. R. Sivior, S. M. Walley, W. G. Proud, and J. E. Field, "The high strain rate compressive behaviour of polycarbonate and polyvinylidene difluoride", *Polymer* **46**:26 (2005), 12546–12555.

[Spitzig and Richmond 1979] W. A. Spitzig and O. Richmond, "Effect of hydrostatic pressure on the deformation behavior of polyethylene and polycarbonate in tension and in compression", *Polym. Eng. Sci.* **19**:16 (1979), 1129–1139.

[Walley and Field 1994] S. M. Walley and J. E. Field, "Strain rate sensitivity of polymers in compression from low to high rates", *DYMAT J.* **1**:3 (1994), 211–227.

[Wang et al. 1994] L. Wang, K. Labibes, Z. Azari, and G. Pluvinage, "Generalization of split Hopkinson bar technique to use viscoelastic bars", *Int. J. Impact Eng.* **15**:5 (1994), 669–686.

[Wood 1967] W. W. Wood, "Experimental mechanics at velocity extremes - very high strain rates", *Exp. Mech.* **7**:10 (1967), 441–446.

[Zhao and Gary 1995] H. Zhao and G. Gary, "A three dimensional analytical solution of the longitudinal wave propagation in an infinite linear viscoelastic cylindrical bar. Application to experimental techniques", *J. Mech. Phys. Solids* **43**:8 (1995), 1335–1348.

Received 19 May 2007. Accepted 23 May 2007.

SAI S. SARVA: saisarva@mit.edu
Department of Mechanical Engineering, Massachusetts Institute of Technology, 77 Massachusetts Avenue, Cambridge, MA 02139, United States

MARY C. BOYCE: mcboyce@mit.edu
Department of Mechanical Engineering, Massachusetts Institute of Technology, 77 Massachusetts Avenue, Cambridge, MA 02139, United States
http://meche.mit.edu/people/faculty/index.html?id=11